Coherent pump-probe spectroscopy in sodium vapor: From electromagnetically induced transparency to parametric amplification

Ken-ichi Takahashi, Nobuhito Hayashi, Hiroaki Kido, Shota Sugimura, Naoya Hombo, and Masaharu Mitsunaga[*]

Graduate School of Science and Technology, Kumamoto University, 2-39-1 Kurokami, Kumamoto, 860-8555, Japan

We have theoretically and experimentally investigated coherent pump-probe spectra for the $3S_{1/2}$-$3P_{1/2}$ $D1$ transition of sodium atomic vapor. Probe transmission spectra in the presence of a coupling beam exhibit dramatic changes depending on experimental conditions. In the weak-excitation, low-atomic-density limit, the spectra are mainly characterized by electromagnetically induced transparency (EIT) and saturated absorption, but for the strong-excitation, high-density case, parametric amplification (PA) is dominant, featuring high probe gain and Stokes-wave generation. We have developed a theory that can explain these two seemingly totally different phenomena (EIT and PA) within the same theoretical framework by manipulating a few experimentally controllable parameters, and have successfully reproduced the observed spectra. Other than the main spectral features, many other interesting physical processes have been predicted and observed.

I. INTRODUCTION

It is well known nowadays that in typical pump-probe spectroscopy using a gaseous atomic vapor with a three-level Λ system, the probe (frequency ω_p) transmission spectra in the presence of a strong-coupling (pump) beam (frequency ω_c) exhibit a wide variety of unique features. On one hand, when coupling power is weak and the atomic density is low, the transmission spectrum is characterized by several, rather broad, saturated absorption dips and peaks and very sharp electromagnetically induced transparency (EIT) peaks [1–5]. The EIT peaks are observed when the two-photon resonance condition ($\omega_p - \omega_c = \pm\omega_{21}$, where ω_{21} is the ground-state hyperfine splitting frequency) is satisfied. This parameter region may be called the EIT region. On the other hand, we have recently reported [6] that, for strong-coupling powers and high atomic densities, which we will call the parametric amplification (PA) region, the initial probe wave is amplified with considerable gain [7] when the two-photon resonance condition is satisfied. Simultaneously, generation of Stokes or anti-Stokes waves (idler waves) due to stimulated Raman scattering (SRS) [8,9], or four-wave mixing [10,11], can be observed with a similar amount of power in the direction that satisfies momentum conservation [12,13]. The parametric gain is high enough to allow parametric oscillation if the system is placed in an external cavity [14]. Ultraslow propagation of the amplified probe and Stokes pulses, often called matched pulses, has also been reported [15–18].

Although these two extreme cases, EIT and PA, provide seemingly totally different spectra, both phenomena should be explained under one unified theory. From this viewpoint, we tried to find a theory that can explain any spectral feature in any region, the EIT region, PA region and any intermediate region, simply by manipulating only a few experimentally controllable parameters: coupling power I_c, coupling detuning frequency δ_c, and atomic density N. We take the $3S_{1/2}$-$3P_{1/2}$ $D1$ transition of a sodium atom for the model system, because the energy structure is rather simple [two hyperfine levels ($F = $

1,2) in both the ground $3S_{1/2}$ and excited $3P_{1/2}$ states], thus we can treat it as a four-level system having two independent Λ systems [4], interacting with three-mode optical fields (probe, coupling, and Stokes) as shown in Fig. 1. This problem can be solved by a combination of the Liouville equations and the rate equations, which finally lead to coupled propagation equations for the probe and Stokes waves, or signal and idler, in terms of PA [19–22]. Theoretical simulations are compared with experimental observations. The agreement between theory and experiment is quite satisfactory, validating our theoretical approach. Moreover, comparison of theory with experiment can elucidate many intriguing problems, such as degenerate four-wave mixing, single-photon resonant SRS, and the splitting and the shift of two-photon resonance peaks. All these interesting topics will be discussed in detail.

In this paper we will first develop, in the next section, a theoretical analysis. Our experimental setup will be briefly mentioned next and then a detailed comparison between theoretical observations and numerical simulations will be presented, along with a discussion about many interesting topics.

II. THEORY

Our aim is to develop a theory that can numerically reproduce experimental observations including two extreme cases, EIT and PA, and can still give enough physical insight into the problem so that it can predict many important issues. Here the numerical fitting should be performed by manipulating only three parameters, the coupling Rabi frequency Ω_c, coupling detuning frequency δ_{c0}, and linear absorption coefficient α_0, which are experimentally controllable and correspond to the coupling power I_c, coupling detuning δ_{c0}, and atomic density N, respectively.

In order to achieve the goal mentioned above, we start by defining the total electric field composed of a probe field (amplitude $\mathcal{E}_p$, frequency ω_p), coupling field ($\mathcal{E}_c, \omega_c$), and Stokes field ($\mathcal{E}_s, \omega_s$), where $\omega_s = \omega_c - \omega_0 = 2\omega_c - \omega_p$ and $\omega_0 \equiv \omega_p - \omega_c$, as [8]

$$E(z,t) = \mathcal{E}_s(z)e^{-i\omega_s t} + \mathcal{E}_c(z)e^{-i\omega_c t} + \mathcal{E}_p(z)e^{-i\omega_p t}. \quad (1)$$
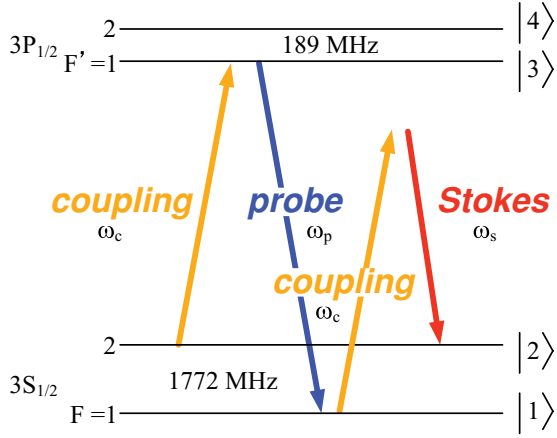
*mitunaga@sci.kumamoto-u.ac.jp

FIG. 1. (Color online) Related energy-level scheme for EIT and PA in sodium vapor.

As for the atomic system, we assume a four-level system as shown in Fig. 1, where the levels 1, 2, 3, and 4 correspond to the $3S_{1/2}$, $F = 1$, $F = 2$, $3P_{1/2}$, $F' = 1$, and $F' = 2$ levels of the sodium atom, respectively. Now we can write down the Liouville equations for the four optical coherences ρ_{13}, ρ_{14}, ρ_{23}, and ρ_{24}, and the ground-state sublevel coherence ρ_{12}. We assume that the excited-state sublevel coherence ρ_{34} can be neglected because it is very short lived compared to ρ_{12} and, therefore, the system is reduced to two independent Λ systems. The Liouville equations can be written as

$$\dot{\rho}_{13} = (i\omega_{31} - \gamma)\rho_{13}$$
$$- \frac{i}{2}\sum_j \Omega^*_{j31}e^{i\omega_j t}n_{13} - \frac{i}{2}\sum_j \Omega^*_{j32}e^{i\omega_j t}\rho_{12},$$

$$\dot{\rho}_{14} = (i\omega_{41} - \gamma)\rho_{14}$$
$$- \frac{i}{2}\sum_j \Omega^*_{j41}e^{i\omega_j t}n_{14} - \frac{i}{2}\sum_j \Omega^*_{j42}e^{i\omega_j t}\rho_{12},$$

$$\dot{\rho}_{23} = (i\omega_{32} - \gamma)\rho_{23}$$
$$- \frac{i}{2}\sum_j \Omega^*_{j32}e^{i\omega_j t}n_{23} - \frac{i}{2}\sum_j \Omega^*_{j31}e^{i\omega_j t}\rho_{21}, \quad (2)$$

$$\dot{\rho}_{24} = (i\omega_{42} - \gamma)\rho_{24}$$
$$- \frac{i}{2}\sum_j \Omega^*_{j42}e^{i\omega_j t}n_{24} - \frac{i}{2}\sum_j \Omega^*_{j41}e^{i\omega_j t}\rho_{21},$$

$$\dot{\rho}_{12} = (i\omega_{21} - \gamma_s)\rho_{12} + \frac{i}{2}\sum_j (\Omega^*_{j31}\rho_{32} + \Omega^*_{j41}\rho_{42})e^{i\omega_j t}$$
$$- \frac{i}{2}\sum_j (\Omega_{j32}\rho_{13} + \Omega_{j42}\rho_{14})e^{-i\omega_j t},$$

where $\omega_{m\ell}$ is the splitting frequency and $n_{\ell m} = n_\ell - n_m$ is the population difference between the level ℓ and the level m, and $\Omega_{jm\ell} = 2p_{m\ell}\mathcal{E}_j/\hbar$ is the Rabi frequency ($j = p,c,s$; $m = 3,4$; and $\ell = 1,2$) with $p_{m\ell}$ being the dipole matrix element. γ and γ_s are the optical and sublevel dephasing rates, respectively.

These equations can be solved by Fourier decomposition of the optical coherences $\rho_{\ell m}$ as

$$\rho_{\ell m}(t) = \rho_{\ell ms}e^{i\omega_s t} + \rho_{\ell mc}e^{i\omega_c t} + \rho_{\ell mp}e^{i\omega_p t}, \quad (3)$$

and the sublevel coherence ρ_{12} as

$$\rho_{12}(t) = \rho_{12u}e^{i\omega_0 t} + \rho_{12d}e^{-i\omega_0 t}. \quad (4)$$

On the other hand the population differences appearing in Eq. (2) can be obtained independently by using the following rate equations for the four populations:

$$\dot{n}_1 = -P_{13}(n_1 - n_3) - P_{14}(n_1 - n_4)$$
$$+ \frac{\Gamma}{2}(n_3 + n_4) - \Gamma_t(n_1 - n_0),$$

$$\dot{n}_2 = -P_{23}(n_2 - n_3) - P_{24}(n_2 - n_4)$$
$$+ \frac{\Gamma}{2}(n_3 + n_4) - \Gamma_t(n_2 - n_0), \quad (5)$$

$$\dot{n}_3 = P_{13}(n_1 - n_3) + P_{23}(n_2 - n_3) - \Gamma n_3 - \Gamma_t n_3,$$
$$\dot{n}_4 = P_{14}(n_1 - n_4) + P_{24}(n_2 - n_4) - \Gamma n_4 - \Gamma_t n_4,$$

where $P_{\ell m}$ represents the optical pumping rate from the ground-state ℓ to the excited-state m level, and $P_{13} = \gamma|\Omega_{c31}|^2/[2\{(\delta_c - \omega_{21})^2 + \gamma^2\}]$, $P_{14} = \gamma|\Omega_{c41}|^2/[2\{(\delta_c - \omega_{21} - \omega_{43})^2 + \gamma^2\}]$, $P_{23} = \gamma|\Omega_{c32}|^2/[2(\delta_c^2 + \gamma^2)]$, and $P_{24} = \gamma|\Omega_{c42}|^2/[2\{(\delta_c - \omega_{43})^2 + \gamma^2\}]$. $\delta_c \equiv \omega_c - \omega_{32}$ is the coupling detuning with respect to the 3-2 transition frequency. Among the four Rabi frequencies, Ω_{c31} is $\sqrt{5}$ times as small as the others in the Na $D1$ line, thus we may rewrite these as $\Omega_{c41} = \Omega_{c42} = \Omega_{c32} = \Omega_c$ and $\Omega_{c31} = \Omega_c/\sqrt{5}$ where Ω_c is the typical Rabi frequency [23,24]. Γ_t is the transit-time decay rate and $n_0 = 1/2$ is the population in thermal equilibrium. The last terms of Eq. (5) guarantee that, without optical pumping, the populations n_1, n_2, n_3, and n_4 are relaxed to their equilibrium values n_0, n_0, 0, and 0, respectively, with the rate Γ_t. In the rate equations above, we assume that the population distribution is solely determined by the coupling beam, neglecting contributions from the probe and Stokes waves. This is equivalent to neglecting higher-order terms for the probe and Stokes waves. We also assume that the coupling field is not depleted and is constant during propagation.

The steady-state solutions of Eq. (5) for n_1, n_2, n_3, and n_4 as functions of δ_c are illustrated in Fig. 2 for $\Omega_c/2\pi = 5$ and 50 MHz. It is clear from Fig. 2 that the role of the coupling beam is to redistribute populations between the two ground-state sublevels 1 and 2 while the excited-state populations are negligible. When the coupling frequency ω_c is resonant to ω_{32} or ω_{42} (left peaks) n_1 dominates n_2, while, when $\omega_c = \omega_{31}$ or ω_{41} (right peaks), n_2 dominates n_1. The linewidths are saturation broadened for the higher coupling Rabi frequency ($\Omega_c/2\pi = 50$ MHz), where the excited-state sublevels are not resolvable.

The recipe for obtaining the final probe and Stokes output spectra is then as follows:

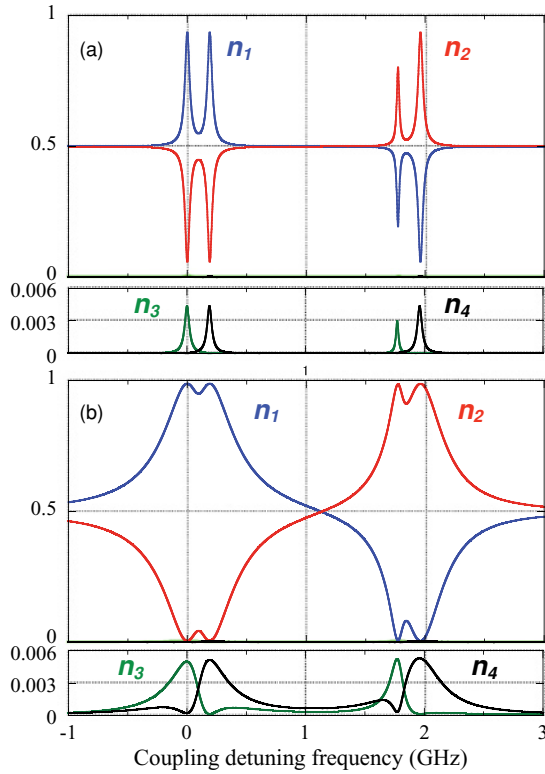(i) obtain steady-state solutions for the rate equations, Eq. (5).

FIG. 2. (Color online) Populations n_1 (blue), n_2 (red), n_3 (green), and n_4 (black) vs the coupling detuning frequency $\delta_c = \omega_c - \omega_{32}$ as solutions of the rate equations Eq. (5). Parameters are the same as those in Table I. (a) $\Omega_c/2\pi = 5$ MHz. (b) $\Omega_c/2\pi = 50$ MHz.

(ii) substitute these values into Eq. (2) to obtain the Fourier components $\rho_{\ell m j}$ (here only the first-order terms in $\mathcal{E}_p$ and $\mathcal{E}_s$ are taken),

(iii) Doppler integrate them by considering inhomogeneous broadening,

(iv) obtain the polarizations with frequencies ω_p and ω_s, and

(v) substitute them into Maxwell's propagation equations for probe and Stokes waves.

We could of course obtain the results by numerically solving all of the Liouville equations [the equations for the populations in addition to those for the coherences given in Eq. (2)]. This numerical method is exact to any higher order of probe and Stokes waves. However, it will not give any analytical expressions nor give any physical insight into the problem. On the other hand, our perturbative approach has a clear physical interpretation, leading to analytical expressions such as (A3) to (A5) and (A8) in the Appendix. Once the analytical expressions are found, each elementary process can be traced out, for example, by using the double-Feynman diagram approach [25]. This was made possible because we assumed that the probe and the Stokes waves are small in amplitude compared to the coupling wave so that nonlinear terms in $\mathcal{E}_p$ and $\mathcal{E}_s$ are neglected [as clearly shown in the next equation, Eq. (6)]. To summarize, our approach is valid and should mimic the experimental results only within the region of weak probe and Stokes waves.

By taking the five steps given above, we reach the following coupled propagation equations for probe and Stokes waves:

$$
\begin{aligned}
\frac{\partial \mathcal{E}_p}{\partial z} &= -\beta_p \mathcal{E}_p + \eta_p \mathcal{E}_s^*, \\
\frac{\partial \mathcal{E}_s}{\partial z} &= -\beta_s \mathcal{E}_s + \eta_s \mathcal{E}_p^*.
\end{aligned}
\tag{6}
$$

The derivation of the above equations and the definitions of the four parameters β_p, η_p, β_s, and η_s are given in the Appendix. Once the above equations are obtained, it is an easy task to solve them with the boundary conditions $\mathcal{E}_p(z = 0) = \mathcal{E}_0$ and $\mathcal{E}_s(z = 0) = 0$, and the solutions at the sample length L are

$$
\mathcal{E}_p(L) = \mathcal{E}_0 \exp[-\sigma L]\left[\cosh(\xi L) - \frac{\beta_p - \beta_s^*}{2\xi}\sinh(\xi L)\right],
$$
$$
\mathcal{E}_s(L) = \mathcal{E}_0 \exp[-\sigma L]\frac{\eta_s^*}{\xi}\sinh(\xi L),
\tag{7}
$$

where $\sigma = (\beta_p + \beta_s^*)/2$ and $\xi = \sqrt{(\beta_p - \beta_s^*)^2 + 4\eta_p\eta_s^*}$. The experimentally observed spectra are the output probe and Stokes intensities, $I_p = |\mathcal{E}_p(L)|^2$ and $I_s = |\mathcal{E}_s(L)|^2$, as a function of the probe detuning frequency, and this is what we try to simulate theoretically.

III. EXPERIMENT

The experimental setup was basically the same as the one we reported before [6,26] as illustrated in Fig. 3, and we mention only the essential parts of the apparatus. We employed two independently tunable ring dye lasers [RDL1 (Coherent CR899-21) and RDL2 (Coherent CR699-21)] for the weak probe beam (typical power ∼1 mW) and the strong-coupling beam (5 to 500 mW), respectively. Both were tuned to the $3S_{1/2}$-$3P_{1/2}$ D_1 transition of the Na atom at 589.6 nm. While the probe frequency was scanned over about 6 GHz, the coupling frequency was fixed. A spatial filter was employed for the probe beam to improve its transverse beam profile, but not for the coupling beam because keeping the high coupling power (∼500 mW) was our first priority. Two beams with linear perpendicular polarizations (probe = vertical and
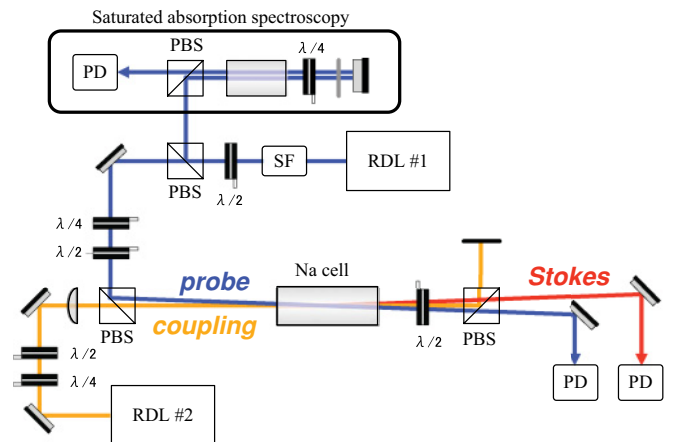

FIG. 3. (Color online) Schematic of the experimental setup: RDL, ring dye laser; PBS, polarizing beam splitter; $\lambda/2$, half-wave plate; $\lambda/4$, quarter-wave plate; PD, photodetector; SF, spatial filter.

coupling = horizontal) impinged noncollinearly (with wave vectors $\vec{k}_p$ and $\vec{k}_c$) on the sample of hot sodium atomic vapor with no buffer gas in a glass cylindrical cell (7.5 cm long). The best crossing angle between $\vec{k}_p$ and $\vec{k}_c$ to give the maximum EIT or PA signal depends on the atomic density, and, for low (high) atomic densities, the angle of 4 mrad (1 mrad) was employed. The intensities of the transmitted probe beam and the newly generated Stokes beam (both are vertically polarized) with $\vec{k}_s = 2\vec{k}_c - \vec{k}_p$ were simultaneously monitored by two photodetectors and then sent to a digitizing oscilloscope. A saturated absorption spectroscopy setup was employed to accurately monitor the probe laser frequency. The atomic density was calculated from the linear absorption spectrum for a weak probe beam and by comparing it with the theoretical curve. (The temperature measurement was not accurate and not dependable.) The coupling power, on the other hand, was simply measured by a power meter. The probe detuning frequency was calibrated by assuming that the separation of the two EIT peaks is $2 \times 1772 = 3544$ MHz. Probe (and Stokes) transmission spectra were obtained for different parameter regions: (i) EIT region, (ii) intermediate region, and (iii) PA region. A detailed comparison with our numerical simulations for the three cases will be given below.

IV. RESULTS

We selected three typical cases for comparing experiment and theory: (i) the EIT region with weak coupling power I_c and low atomic density N, (ii) the intermediate region with strong I_c and low N, and (iii) the PA region with strong I_c and high N. The region with weak I_c and high N is not of interest because it simply gives an opaque medium with little spectroscopic features. All the experimental parameters and all the parameters used in the simulation are tabulated in Table I, where the peak optical density D, defined as $D \equiv \log_{10}[I_p(0)/I_p(L)]$, without the coupling beam is proportional to α_0. The linear absorption linewidth $\gamma/2\pi$ is set as 8 MHz taking into account the two independent laser linewidths in addition to its original linewidth 5 MHz. The Doppler widths of the $D1$ transition of the Na atom are calculated to be $\omega_D/2\pi = 1650$ MHz at 200 °C and 1730 MHz at 250 °C and can be roughly approximated as constant. It should be mentioned that, in the simulation, only three parameters, the coupling Rabi frequency Ω_c, coupling detuning δ_{c0}, and absorption coefficient α_0, are changed for the three regions and all the remaining parameters are fixed, implying that the above three are the only experimentally controllable parameters. In the following the experimental results and the simulation results will be shown.

A. EIT region

The probe absorption spectra in this region are shown in Fig. 4 for the experiment (top) and the theoretical simulation (bottom). In this region, the spectra are characterized by rather broad saturated absorption (SA) peaks and very sharp EIT peaks [4,5] indicated by arrows in Fig. 4. The SA signals have nine peaks and dips with linewidths of $2\gamma/2\pi \sim 16$ MHz when Ω_c is small. Among the nine SA signals, three of them are peaks (quenching of absorption) located at $\omega_p = \omega_c, \omega_c \pm \omega_{43}$
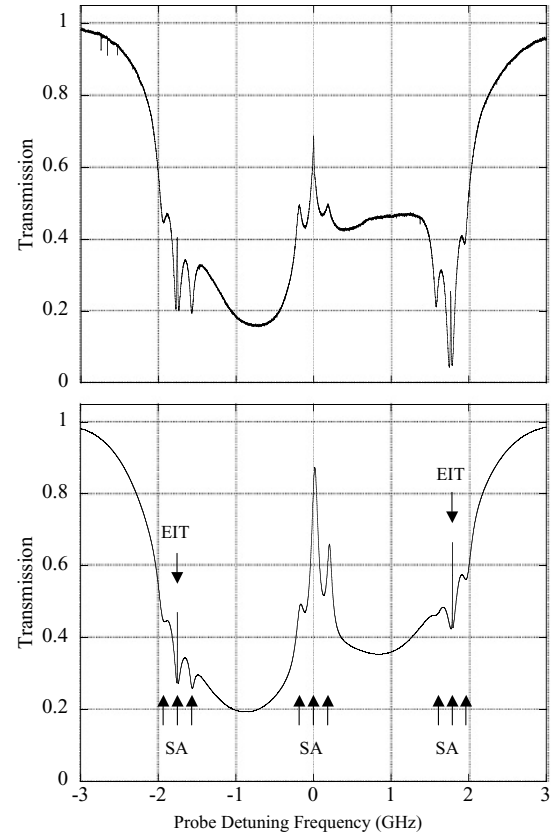

FIG. 4. Probe transmission spectra in the EIT region. Top: experiment. Bottom: theory.

in the central region, and the other six are dips (extra absorption) at $\omega_p = \omega_c \pm \omega_{21}, \omega_c \pm \omega_{21} \pm \omega_{43}$ in the left and right wings. The physical origin of these signals is ground-state population redistribution by the coupling beam (see Fig. 2), and in this sense this is quite similar to ordinary saturated absorption spectroscopy, or Lamb-dip spectroscopy [27–29], in which case two counterpropagating beams from the same laser are applied to the sample.

In contrast to the SA peaks, the EIT peaks are identified at $\omega_p = \omega_c \pm \omega_{21}$ as very sharp upward signals. The linewidths ($2\gamma_s/2\pi \sim 1.4$ MHz) are much smaller than the saturated absorption linewidths, and therefore the SA and EIT peaks are easily distinguishable. The numerical simulation was performed with the parameters given in Table I and, although each peak height does not exactly match, the agreement between experimental observation and theory is quite satisfactory.

B. Intermediate region

Figure 5 shows the case of the intermediate region for strong excitation and low atomic density. Here all the saturated absorption signals observed in Fig. 4 disappear. This is because of the saturation broadening of the level populations seen in Fig. 2, since the linewidth of the saturated absorption signal is given by $2\sqrt{\gamma^2 + \Omega_c^2 \gamma / \Gamma}$ and, for sufficiently large Ω_c, it is proportional to Ω_c. On the other hand, the EIT signals became very pronounced with increasing magnitudes but with no apparent broadening. All these features can be nicely reproduced in the theoretical simulation. The noise

TABLE I. Parameters used in the experiment and the simulation.

		EIT	Intermediate	PA
Expt.	I_c (mW)	13	270	480
	I_p (mW)	2.7	0.55	1.5
	T (°C)	185	175	215
	N (cm^{-3})	3.8×10^{10}	2.1×10^{10}	2.0×10^{11}
Sim.	$\Omega_c/2\pi$ (MHz)	14	75	100
	$\delta_{c0}/2\pi$ (MHz)	1000	1020	100
	α_0 (cm^{-1})	15	9.5	330
	D	0.72	0.46	16
	$\gamma/2\pi$ (MHz)		8	
	$\Gamma/2\pi$ (MHz)		10	
	$\gamma_s/2\pi$ (MHz)		0.7	
	$\Gamma_t/2\pi$ (MHz)		0.1	
	$\omega_D/2\pi$ (MHz)		1600	
	L (cm)		7.5	
	$\omega_{21}/2\pi$ (MHz)		1772	
	$\omega_{34}/2\pi$ (MHz)		189	

modulation, or "ripple," appearing in the experimental signal is spurious. It is due to cell-heater switching and it should be averaged out. Up to this point the Stokes wave has been negligible.
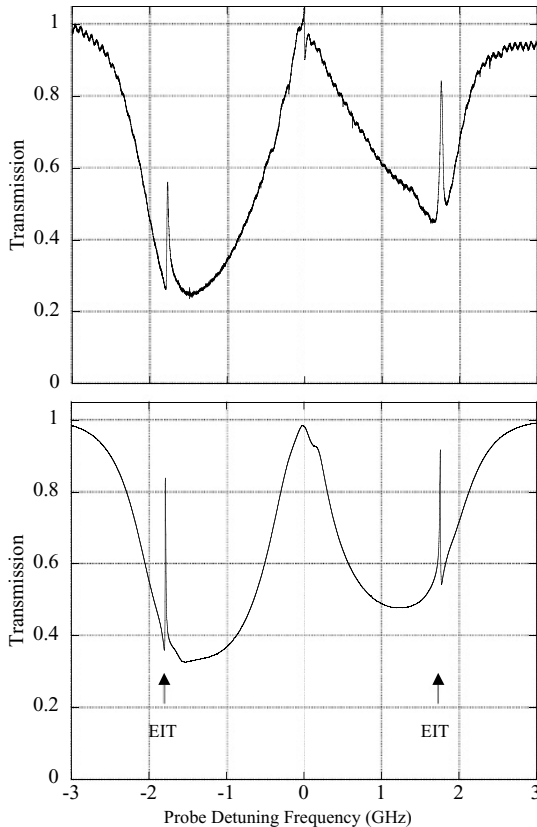

FIG. 5. Probe transmission spectra in the intermediate region. Top: experiment. Bottom: theory.
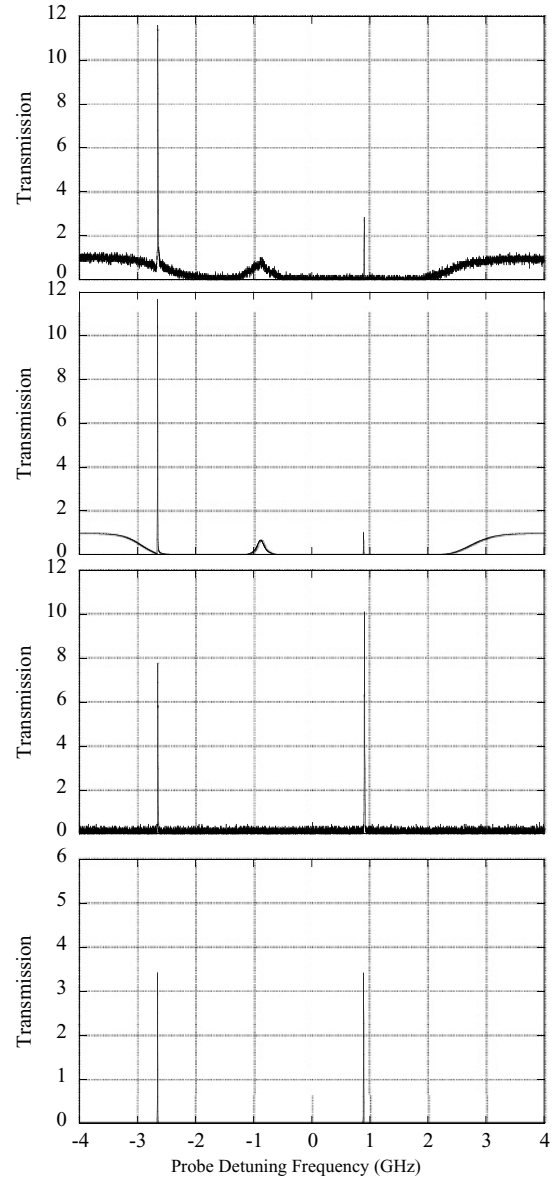

FIG. 6. Probe transmission spectra in the PA region. From top to bottom: probe experiment, probe theory, Stokes experiment, and Stokes theory.

C. PA region

The transmission spectra in the PA region show a dramatic change compared to the two previous examples and are shown in Fig. 6. Experimentally, the probe wave is amplified with large gain reaching 12 when the probe frequency is in the wing of the absorption line. The other resonance appearing in the middle of the absorption had a smaller gain of about 3, implying that too much absorption suppresses gain. A broad saturated absorption peak was observed at $\omega_p = \omega_c$. In addition, in this region, the generation of the Stokes wave (idler wave) is very pronounced. The output Stokes power is similar to that of probe, and this time the two sharp peaks have almost the same magnitude. All these basic features are satisfactorily reproduced by the numerical simulation as shown also in Fig. 6, except that the Stokes magnitudes are much smaller in the simulation.
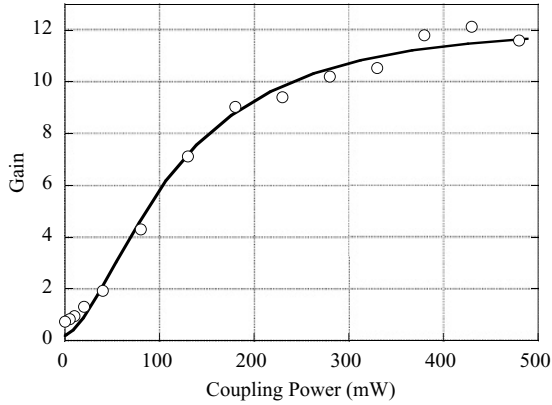
FIG. 7. Coupling power dependence of probe gain. Solid line, simulation. Open circles, experiment. Probe power $I_p = 1.5$ mW. Temperature $T = 215\,^{\circ}$C. Density $N = 2.0 \times 10^{11}$ cm^{-3}.

The growth of the probe gain at the two-photon resonance peak (left peak in Fig. 6) from the EIT region to the PA region as a function of the coupling power I_c is plotted in Fig. 7 both for the experimental results (open circles) and the simulation (solid line). For small I_c the gain is of course less than 1, but eventually reaches up to 12 and becomes saturated. The theoretical simulation reproduces the observations quite well.

V. DISCUSSION

In this section we list all the important spectral features and topics observed either in experiment or theory.

A. Degenerate four-wave mixing

There is one spectral feature that is always observed and is quite often very pronounced experimentally but cannot be reproduced by the simulation. It is the degenerate four-wave mixing signal observed when $\omega_p = \omega_c$ [4]. It is observed, for example, in Fig. 5 as a very sharp peak (sometimes dispersion type) at the center of the spectrum. This signal can be regarded as diffraction of the coupling beam by the stationary grating produced by the coupling and the probe beams when $\omega_p = \omega_c$. The reason why it is not theoretically reproducible is because, in our approach, we employ a Fourier expansion with the sideband frequency ω_0, as written in Eqs. (3) and (4). This approximation collapses when the sideband frequency ω_0 becomes zero, when probe, coupling, and Stokes waves all become degenerate.

B. Half resonances

In contrast to the previous topic, there is one spectral feature that always appears in simulations but has not been observed experimentally. It is what we call a half resonance. As shown in Fig. 8 for a simulation with very high Ω_c, we have six small resonances appearing at almost half the way to the main resonances $\omega_p = \omega_c \pm \omega_{21}$ in both the probe and Stokes spectra. These resonances are found to be located at $\omega_p = \omega_c \pm \omega_{21}/2$ and $\omega_c \pm (\omega_{21} \pm \omega_{43})/2$. These half resonances can be interpreted as follows. If we take a close look at the coefficients such as c_{ps} in Eqs. (A2), (A3), (A4), and (A5), we notice that there are three resonance denominators that contribute to the
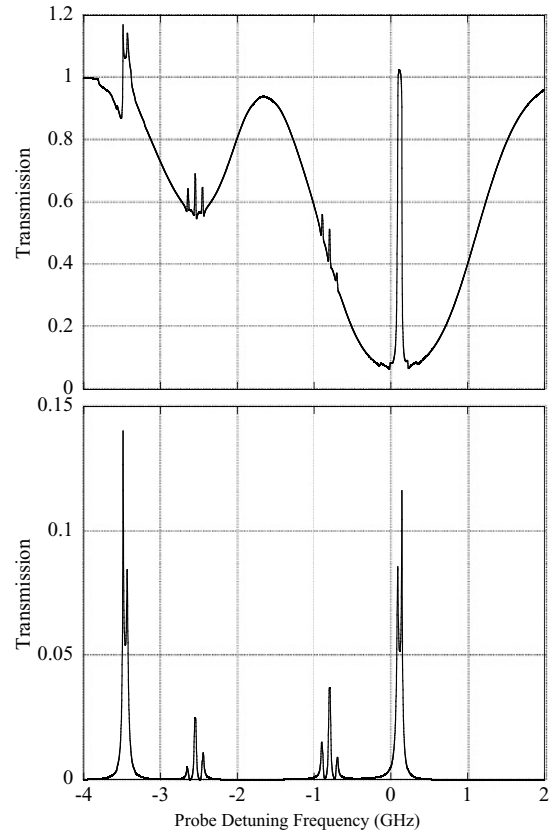

FIG. 8. Existence of half resonances and splitting of EIT resonances in the numerical simulation. Top: probe output. Bottom: Stokes output. Parameters: $\Omega_c/2\pi = 200$ MHz, $\delta_{c0}/2\pi = 100$ MHz, and $\alpha_0 = 12$ cm^{-1}.

signal magnitude. Among them, two of them are single-photon resonances (typical example: $\omega_p = \omega_{31}$ and $\omega_s = \omega_{32}$) and the other one is a two-photon resonance (typical example: $\omega_p - \omega_c = \omega_{21}$). There is no way to satisfy these three conditions simultaneously. Ordinary EIT signals satisfy one
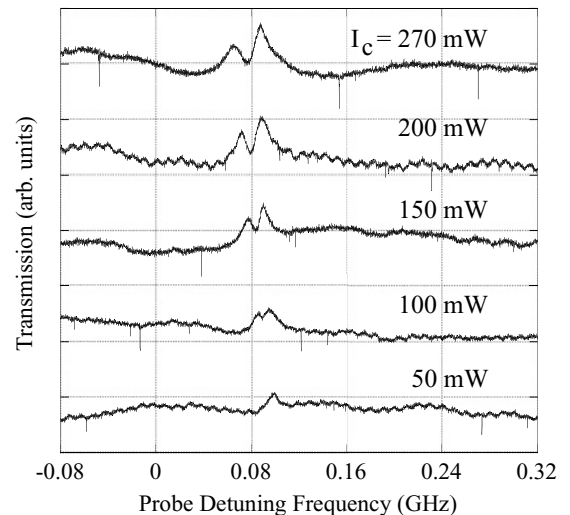

FIG. 9. Experimentally observed splitting of the EIT resonance peak (left peak). From top to bottom, coupling power $I_c = 270, 200, 150, 100,$ and 50 mW. Temperature, $T = 175\,^{\circ}$C.
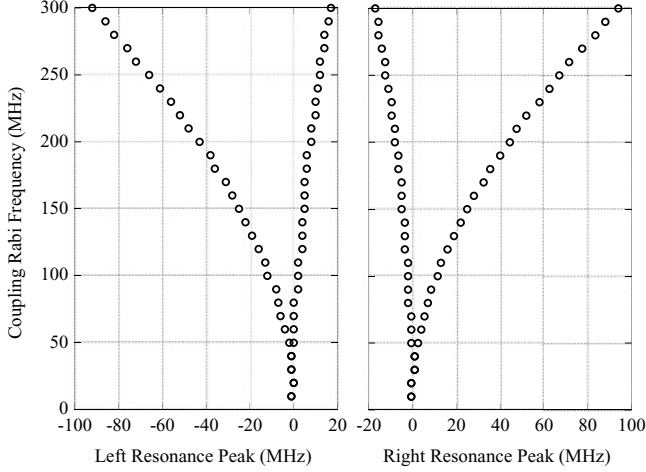
FIG. 10. Numerically calculated peak positions of the left peak and the right peak of the main resonances as a function of the coupling Rabi frequency Ω_c. Parameters are the same as the ones in Fig. 8.

single-photon resonance and one two-photon resonance, for example, $\omega_p = \omega_{31}$ and $\omega_p - \omega_c = \omega_{21}$. But one has the other option that two single-photon resonances are satisfied sacrificing one two-photon resonance. These resonances are much smaller than the main resonances as shown in Fig. 8 but become pronounced when Ω_c is large. They have not been observed experimentally, probably due to our low detection sensitivity.

C. Splitting and shift of EIT peaks

In Fig. 8 we clearly observe that the left peak at -3444 MHz and the right peak at 100 MHz of the main EIT resonances are split into two. (They are more pronounced in the Stokes spectrum.) This type of splitting was also observed experimentally, as shown in Fig. 9 for the left EIT peak, where peak splitting at high coupling powers is obvious. At the same time we find that the peaks started to shift toward the left. The behavior of the left peak and the right peak positions as a function of the coupling Rabi frequency Ω_c is numerically calculated and visualized in Fig. 10. The magnitude of the splitting in Fig. 10 agrees roughly with that in Fig. 9. It is clear from Fig. 10 that the left and right peak shifts and splittings are very symmetrical. While the shifts of the inner peaks are small, the outer peaks shift further toward the outside. This shift may be attributed to the light shifts of level 1 (right peak) and level 2 (left peak) due to the strong-coupling beam, but the detailed mechanisms of this shift and splitting are yet to be investigated.

VI. CONCLUSIONS

We have developed a theory for a four-level double-Λ system to explain various experimental observations in the coherent pump-probe spectroscopy for the sodium $D1$ transition. Numerical simulations based upon our theory can reproduce the experimental results reasonably well in every parameter region: from the EIT region for the weak-excitation low-density limit to the PA region for the strong-excitation high-density limit. Other than this, our theory provided an

opportunity to consider various spectroscopic features that appear only in theoretical spectra (half resonances), or only in experimental spectra (degenerate four-wave mixing), or both of the spectra (splittings and shifts of EIT resonances), as mentioned in the previous section. These spectral features will in turn drive further investigation into these yet-to-be-explored problems.

This type of approach may be applied to the optical data storage problem [30] or the coherent Raman beat problem [31], where transient solutions are obtained in the four-level configuration, and a much more sophisticated and quantitative comparison between theory and experiment will become possible as here. Another direct application of this theory will be the slow-light problem [15–18]. Both in the EIT region and in the PA region, the input probe pulse and also the generated Stokes pulse are reported to be slowed considerably in the presence of the continuous coupling wave. Since, theoretically, the temporal profile of the probe (Stokes) pulse is simply a Fourier transform of the probe (Stokes) output spectrum, a detailed comparison of theory and experiment in every parameter region should be straightforward with some effort.

APPENDIX

Maxwell's propagation equations for the probe and the Stokes waves are written as

$$
\begin{aligned}
\frac{\partial \mathcal{E}_p}{\partial z} &= \frac{ik}{2\epsilon_0} \mathcal{P}_p \\
&= \frac{ikN}{2\epsilon_0}(p_{13}\rho_{31p} + p_{23}\rho_{32p} + p_{14}\rho_{41p} + p_{24}\rho_{42p}), \\
\frac{\partial \mathcal{E}_s}{\partial z} &= \frac{ik}{2\epsilon_0} \mathcal{P}_s \\
&= \frac{ikN}{2\epsilon_0}(p_{13}\rho_{31s} + p_{23}\rho_{32s} + p_{14}\rho_{41s} + p_{24}\rho_{42s}),
\end{aligned}
\tag{A1}
$$

where $\mathcal{P}_p$ and $\mathcal{P}_s$ are the polarizations oscillating at frequencies ω_p and ω_p, respectively, and N is the atomic density. By solving Eq. (2) for $\rho_{\ell mp}$ and $\rho_{\ell mp}$ and substituting them into Eq. (A1), we obtain the following propagation equations:

$$
\begin{aligned}
\frac{\partial \mathcal{E}_p}{\partial z} &= -\frac{1}{2}\alpha_p \mathcal{E}_p + c_{pp}|\mathcal{E}_c|^2 \mathcal{E}_p + c_{ps}\mathcal{E}_c^2 \mathcal{E}_s^*, \\
\frac{\partial \mathcal{E}_s}{\partial z} &= -\frac{1}{2}\alpha_s \mathcal{E}_s + c_{ss}|\mathcal{E}_c|^2 \mathcal{E}_s + c_{sp}\mathcal{E}_c^2 \mathcal{E}_p^*.
\end{aligned}
\tag{A2}
$$

Among the three terms of the right-hand sides, the first terms represent linear absorption, the second terms correspond to EIT, and the third terms are parametric coupling between the probe and Stokes waves. The coefficients α_p, α_s, c_{pp}, c_{ps}, c_{sp}, and c_{ss} are expressed as

$$
\alpha_p = \alpha_0 \gamma \left(\frac{|\epsilon_{31}|^2}{\gamma_{p31}} n_{13} + \frac{|\epsilon_{32}|^2}{\gamma_{p32}} n_{23} + \frac{|\epsilon_{41}|^2}{\gamma_{p41}} n_{14} + \frac{|\epsilon_{42}|^2}{\gamma_{p42}} n_{24} \right),
$$

$$
\alpha_s = \alpha_0 \gamma \left(\frac{|\epsilon_{31}|^2}{\gamma_{s31}} n_{13} + \frac{|\epsilon_{32}|^2}{\gamma_{s32}} n_{23} + \frac{|\epsilon_{41}|^2}{\gamma_{s41}} n_{14} + \frac{|\epsilon_{42}|^2}{\gamma_{s42}} n_{24} \right),
$$

$$
c_{pp} = \frac{kNp^4}{2\epsilon_0\hbar^3} \left(\frac{c_{pp1}}{\gamma_u} + \frac{c_{pp2}}{\gamma_d} \right),
$$

$$c_{ps} = \frac{kNp^4}{2\epsilon_0\hbar^3}\left(\frac{c_{ps1}}{\gamma_u} + \frac{c_{ps2}}{\gamma_d}\right),$$

$$c_{sp} = \frac{kNp^4}{2\epsilon_0\hbar^3}\left(\frac{c_{sp1}}{\gamma_d^*} + \frac{c_{sp2}}{\gamma_u^*}\right),$$

$$c_{ss} = \frac{kNp^4}{2\epsilon_0\hbar^3}\left(\frac{c_{ss1}}{\gamma_d^*} + \frac{c_{ss2}}{\gamma_u^*}\right). \tag{A3}$$

Here $\alpha_0 = \frac{kNp^2}{\epsilon_0\hbar\gamma}$ is the linear absorption coefficient without Doppler broadening and $\epsilon_{m\ell} = p_{m\ell}/p$ denotes the relative transition amplitude from ℓ to m. γ_u and γ_d in Eq. (A3) are

defined as

$$\gamma_u = \gamma_s - i(\omega_0 - \omega_{21})$$
$$+ \frac{\Omega_c^2}{4}\left(\frac{|\epsilon_{31}|^2}{\gamma_{s32}^*} + \frac{|\epsilon_{41}|^2}{\gamma_{s42}^*} + \frac{|\epsilon_{32}|^2}{\gamma_{p31}} + \frac{|\epsilon_{42}|^2}{\gamma_{p41}}\right),$$

$$\gamma_d = \gamma_s - i(\omega_0 + \omega_{21})$$
$$+ \frac{\Omega_c^2}{4}\left(\frac{|\epsilon_{31}|^2}{\gamma_{p32}} + \frac{|\epsilon_{41}|^2}{\gamma_{p42}} + \frac{|\epsilon_{32}|^2}{\gamma_{s31}^*} + \frac{|\epsilon_{42}|^2}{\gamma_{s41}^*}\right), \tag{A4}$$

where $\gamma_{jm\ell} = \gamma - i(\omega_j - \omega_{m\ell})$ ($j = p,c,s; m = 3,4$; and $\ell = 1,2$). The eight coefficients $c_{pp1}, c_{pp2}, c_{ss1}, c_{ss2}, c_{ps1}, c_{ps2}, c_{sp1}$, and c_{sp2} are given by

$$c_{pp1} = \left(\frac{|\epsilon_{31}|^2|\epsilon_{32}|^2}{\gamma_{p31}} + \frac{\epsilon_{31}\epsilon_{14}\epsilon_{42}\epsilon_{23}}{\gamma_{p41}}\right)\left(\frac{n_{13}}{\gamma_{p31}} + \frac{n_{23}}{\gamma_{c32}^*}\right) + \left(\frac{|\epsilon_{41}|^2|\epsilon_{42}|^2}{\gamma_{p41}} + \frac{\epsilon_{32}\epsilon_{24}\epsilon_{41}\epsilon_{13}}{\gamma_{p31}}\right)\left(\frac{n_{14}}{\gamma_{p41}} + \frac{n_{24}}{\gamma_{c42}^*}\right),$$

$$c_{pp2} = \left(\frac{|\epsilon_{31}|^2|\epsilon_{32}|^2}{\gamma_{p32}} + \frac{\epsilon_{13}\epsilon_{32}\epsilon_{24}\epsilon_{41}}{\gamma_{p42}}\right)\left(\frac{n_{13}}{\gamma_{c31}^*} + \frac{n_{23}}{\gamma_{p32}}\right) + \left(\frac{|\epsilon_{41}|^2|\epsilon_{42}|^2}{\gamma_{p42}} + \frac{\epsilon_{31}\epsilon_{14}\epsilon_{42}\epsilon_{23}}{\gamma_{p32}}\right)\left(\frac{n_{14}}{\gamma_{c41}^*} + \frac{n_{24}}{\gamma_{p42}}\right),$$

$$c_{ss1} = \left(\frac{|\epsilon_{31}|^2|\epsilon_{32}|^2}{\gamma_{s31}} + \frac{\epsilon_{31}\epsilon_{14}\epsilon_{42}\epsilon_{23}}{\gamma_{s41}}\right)\left(\frac{n_{13}}{\gamma_{s31}} + \frac{n_{23}}{\gamma_{c32}^*}\right) + \left(\frac{|\epsilon_{41}|^2|\epsilon_{42}|^2}{\gamma_{s41}} + \frac{\epsilon_{32}\epsilon_{24}\epsilon_{41}\epsilon_{13}}{\gamma_{s31}}\right)\left(\frac{n_{14}}{\gamma_{s41}} + \frac{n_{24}}{\gamma_{c42}^*}\right),$$

$$c_{ss2} = \left(\frac{|\epsilon_{31}|^2|\epsilon_{32}|^2}{\gamma_{s32}} + \frac{\epsilon_{13}\epsilon_{32}\epsilon_{24}\epsilon_{41}}{\gamma_{s42}}\right)\left(\frac{n_{13}}{\gamma_{c31}^*} + \frac{n_{23}}{\gamma_{s32}}\right) + \left(\frac{|\epsilon_{41}|^2|\epsilon_{42}|^2}{\gamma_{s42}} + \frac{\epsilon_{31}\epsilon_{14}\epsilon_{42}\epsilon_{23}}{\gamma_{s32}}\right)\left(\frac{n_{14}}{\gamma_{c41}^*} + \frac{n_{24}}{\gamma_{s42}}\right),$$

$$c_{ps1} = \left(\frac{|\epsilon_{31}|^2|\epsilon_{32}|^2}{\gamma_{p31}} + \frac{\epsilon_{31}\epsilon_{14}\epsilon_{42}\epsilon_{23}}{\gamma_{p41}}\right)\left(\frac{n_{13}}{\gamma_{c31}} + \frac{n_{23}}{\gamma_{s32}^*}\right) + \left(\frac{|\epsilon_{41}|^2|\epsilon_{42}|^2}{\gamma_{p41}} + \frac{\epsilon_{32}\epsilon_{24}\epsilon_{41}\epsilon_{13}}{\gamma_{p31}}\right)\left(\frac{n_{14}}{\gamma_{c41}} + \frac{n_{24}}{\gamma_{s42}^*}\right),$$

$$c_{ps2} = \left(\frac{|\epsilon_{31}|^2|\epsilon_{32}|^2}{\gamma_{p32}} + \frac{\epsilon_{13}\epsilon_{32}\epsilon_{24}\epsilon_{41}}{\gamma_{p42}}\right)\left(\frac{n_{13}}{\gamma_{s31}^*} + \frac{n_{23}}{\gamma_{c32}}\right) + \left(\frac{|\epsilon_{41}|^2|\epsilon_{42}|^2}{\gamma_{p42}} + \frac{\epsilon_{31}\epsilon_{14}\epsilon_{42}\epsilon_{23}}{\gamma_{p32}}\right)\left(\frac{n_{14}}{\gamma_{s41}^*} + \frac{n_{24}}{\gamma_{c42}}\right),$$

$$c_{sp1} = \left(\frac{|\epsilon_{31}|^2|\epsilon_{32}|^2}{\gamma_{s31}} + \frac{\epsilon_{31}\epsilon_{14}\epsilon_{42}\epsilon_{23}}{\gamma_{s41}}\right)\left(\frac{n_{13}}{\gamma_{c31}} + \frac{n_{23}}{\gamma_{p32}^*}\right) + \left(\frac{|\epsilon_{41}|^2|\epsilon_{42}|^2}{\gamma_{s41}} + \frac{\epsilon_{32}\epsilon_{24}\epsilon_{41}\epsilon_{13}}{\gamma_{s31}}\right)\left(\frac{n_{14}}{\gamma_{c41}} + \frac{n_{24}}{\gamma_{p42}^*}\right),$$

$$c_{sp2} = \left(\frac{|\epsilon_{31}|^2|\epsilon_{32}|^2}{\gamma_{s32}} + \frac{\epsilon_{13}\epsilon_{32}\epsilon_{24}\epsilon_{41}}{\gamma_{s42}}\right)\left(\frac{n_{13}}{\gamma_{p31}^*} + \frac{n_{23}}{\gamma_{c32}}\right) + \left(\frac{|\epsilon_{41}|^2|\epsilon_{42}|^2}{\gamma_{s42}} + \frac{\epsilon_{31}\epsilon_{14}\epsilon_{42}\epsilon_{23}}{\gamma_{s32}}\right)\left(\frac{n_{14}}{\gamma_{p41}^*} + \frac{n_{24}}{\gamma_{c42}}\right). \tag{A5}$$

Finally, in Eq. (A2) all the coefficients are Doppler averaged as, for example,

$$\beta_p = \langle\beta_p(\delta_D)\rangle = \int d\delta_D \mathcal{G}(\delta_D)\beta_p(\delta_D), \tag{A6}$$

with δ_D being the Doppler shift and $\mathcal{G}(\delta_D)$ being the Doppler distribution having the Doppler width ω_D,

$$\mathcal{G}(\delta_D) = \frac{2\sqrt{\ln 2}}{\sqrt{\pi}\omega_D}\exp\left[-\left(\frac{2\sqrt{\ln 2}\delta_D}{\omega_D}\right)^2\right]. \tag{A7}$$

In performing Doppler averaging, the probe and coupling frequencies in all the coefficients have to be Doppler shifted as $\omega_p \to \omega_{p0} - \delta_D$ and $\omega_c \to \omega_{c0} - \delta_D$, where ω_{p0} and ω_{c0} are the original probe and coupling frequencies. Considering these facts, the four parameters appearing in the propagation equations Eq. (6) are obtained as

$$\beta_p = \left\langle\frac{1}{2}\alpha_p - \frac{1}{8}\alpha_0\gamma|\Omega_c|^2\left(\frac{c_{pp1}}{\gamma_u} + \frac{c_{pp2}}{\gamma_d}\right)\right\rangle, \quad \beta_s = \left\langle\frac{1}{2}\alpha_s - \frac{1}{8}\alpha_0\gamma|\Omega_c|^2\left(\frac{c_{ss1}}{\gamma_d^*} + \frac{c_{ss2}}{\gamma_u^*}\right)\right\rangle, \quad \eta_p = \left\langle\frac{1}{8}\alpha_0\gamma\Omega_c^2\left(\frac{c_{ps1}}{\gamma_u} + \frac{c_{ps2}}{\gamma_d}\right)\right\rangle,$$

$$\eta_s = \left\langle\frac{1}{8}\alpha_0\gamma\Omega_c^2\left(\frac{c_{sp1}}{\gamma_d^*} + \frac{c_{sp2}}{\gamma_u^*}\right)\right\rangle. \tag{A8}$$

[1] K.-J. Boller, A. Imamoğlu, and S. E. Harris, Phys. Rev. Lett. **66**, 2593 (1991).

[2] J. E. Field, K. H. Hahn, and S. E. Harris, Phys. Rev. Lett. **67**, 3062 (1991).

[3] D. J. Fulton, S. Shepherd, R. R. Moseley, B. D. Sinclair, and M. H. Dunn, Phys. Rev. A **52**, 2302 (1995).

[4] V. Wong, R. W. Boyd, C. R. Stroud Jr., R. S. Bennink, and A. M. Marino, Phys. Rev. A **68**, 012502 (2003).

[5] S. Mitra, M. M. Hossain, B. Ray, P. N. Ghosh, S. Cartaleva, and D. Slavov, Opt. Commun. **283**, 1500 (2010).

[6] K. I. Harada, K. Mori, J. Okuma, N. Hayashi, and M. Mitsunaga, Phys. Rev. A **78**, 013809 (2008).

[7] C. F. McCormick, V. Boyer, E. Arimondo, and P. D. Lett, Opt. Lett. **32**, 178 (2007).

[8] V. Wong, R. S. Bennink, A. M. Marino, R. W. Boyd, C. R. Stroud Jr., and F. A. Narducci, Phys. Rev. A **70**, 053811 (2004).

[9] R. S. Bennink, A. M. Marino, V. Wong, R. W. Boyd, and C. R. Stroud Jr., Phys. Rev. A **72**, 023827 (2005).

[10] D. A. Braje, V. Balić, S. Goda, G. Y. Yin, and S. E. Harris, Phys. Rev. Lett. **93**, 183601 (2004).

[11] G. Q. Yang, P. Xu, J. Wang, Y. Zhu, and M. S. Zhan, Phys. Rev. A **82**, 045804 (2010).

[12] J. A. Giordmaine and R. C. Miller, Phys. Rev. Lett. **14**, 973 (1965).

[13] A. F. Huss, N. Peer, R. Lammeggar, E. A. Korsunsky, and L. Windholz, Phys. Rev. A **63**, 013802 (2000).

[14] J. Okuma, N. Hayashi, A. Fujisawa, M. Mitsunaga, and K. Harada, Opt. Lett. **34**, 698 (2009).

[15] V. Boyer, C. F. McCormick, E. Arimondo, and P. D. Lett, Phys. Rev. Lett. **99**, 143601 (2007).

[16] I. Novikova, D. F. Phillips, and R. L. Walsworth, Phys. Rev. Lett. **99**, 173604 (2007).

[17] J. Okuma, N. Hayashi, A. Fujisawa, and M. Mitsunaga, Opt. Lett. **34**, 1654 (2009).

[18] A. Fujisawa, N. Hayashi, K. Takahashi, H. Kido, and M. Mitsunaga, J. Opt. Soc. Am. B **27**, 1280 (2010).

[19] M. D. Lukin, M. Fleischhauer, A. S. Zibrov, H. G. Robinson, V. L. Velichansky, L. Hollberg, and M. O. Scully, Phys. Rev. Lett. **79**, 2959 (1997).

[20] A. S. Zibrov, M. D. Lukin, and M. O. Scully, Phys. Rev. Lett. **83**, 4049 (1999).

[21] K. I. Harada, T. Kanbashi, M. Mitsunaga, and K. Motomura, Phys. Rev. A **73**, 013807 (2006).

[22] G. S. Agarwal, T. N. Dey, and D. J. Gauthier, Phys. Rev. A **74**, 043805 (2006).

[23] M. Têtu, N. Cyr, B. Villeneuve, S. Thériault, M. Breton, and P. Tremblay, IEEE Trans. Instrum. Meas. **40**, 191 (1991).

[24] H. J. Metcalf and P. van der Straten, *Laser Cooling and Trapping* (Springer, New York, 1999).

[25] M. Mitsunaga and N. Imoto, Phys. Rev. A **59**, 4773 (1999).

[26] N. Hayashi, A. Fujisawa, H. Kido, K. Takahashi, and M. Mitsunaga, J. Opt. Soc. Am. B **27**, 1645 (2010).

[27] P. Meystre and M. Sargent III, *Elements of Quantum Optics* (Springer, Berlin, 2007).

[28] W. Demtröder, *Laser Spectroscopy* (Springer, Berlin, 2008), Vol. 2.

[29] J. Duan, X. Qi, X. Zhou, and X. Chen, Opt. Lett. **36**, 561 (2011).

[30] D. F. Phillips, A. Fleischhauer, A. Mair, R. L. Walsworth, and M. D. Lukin, Phys. Rev. Lett. **86**, 783 (2001).

[31] K. Harada, K. Motomura, T. Koshimizu, H. Ueno, and M. Mitsunaga, J. Opt. Soc. Am. B **22**, 1105 (2005).